ISSN 1063-7826, Semiconductors, 2025, Vol. 59, No. 2, pp. 190–202. © Pleiades Publishing, Ltd., 2025.

Tuning the Structural, Electronic, and Optical Properties by the Incorporation of Sb into *n*-ZnO Semiconductor via DFT Calculation

Mosfiqur Rahman[a,b,*] (ORCID: 0000-0002-4117-7756), Md. Kamruzzaman[b], Md. Al Helal[b], and Md. Nurul Huda Liton[b]

[a] *Department of Physics, Uttara University, Holding 77, Beribadh Road, Turag, Uttara, Dhaka, 1230 Bangladesh*

[b] *Department of Physics, Begum Rokeya University, Rangpur, 5400 Bangladesh*

**e-mail: mosfiqur56@gmail.com*

Received October 15, 2024; revised December 18, 2024; accepted December 19, 2024

Abstract—The geometry optimization, structural characteristics, electronic, and optical properties of the pure and Sb doped hexagonal wurtzite ZnO have been investigated using the first principles calculations ultrasoft pseudopotential approach of the plane wave upon the basis of the Density Functional Theory (DFT). According to the estimated results, the volume of ZnO doped with Sb exhibits *p*-type degenerate semiconductor characteristics and acts as a deep acceptor. Furthermore, a peak of Sb-5*p* states occupied close to the Fermi level forms, which leads the optical band gap to shrink and the Density of States (DOS) to shift towards lower energy. Additionally, it is discovered that our findings agree well with those of other experiments. A more precise monitoring and control during the formation of ZnO, *p*-type materials is also made possible by the computed results. The formation of the *p*-type conductivity of Sb doped ZnO is evidenced by the dielectric constants and photoconductivity spectra, which are in accordance with the available experimental and theoretical reports.

Keywords: First principles calculations, ZnO, band gap, optical properties, *p*-type conductivity

DOI: 10.1134/S1063782624602024

1. INTRODUCTION

Zinc oxide (ZnO) thin films, both pure and doped, have been found to be a highly transparent binary semiconductor material with a large exciton binding energy (60 meV) [1] at room temperature, and often has a wide energy band gap (3.37 eV) [2]. In light of the advancements in thin film fabrication techniques, ZnO has garnered more interest recently, opening up a wider range of potential device applications for this wide band gap semiconductor [3]. Due to the growing demand for nontoxic, abundant, and superior electrical, optical, and magnetic properties in short wavelength devices [4–7], ZnO has become widely recognized as a material that shows great promise for many different kinds of purposes. In fact, it has discovered a wide range of applications, including surface acoustic wave devices, solar cells, phosphors, transparent conducting films, Ultra-violet (UV) resistive coatings, bio-sensors, transducers, varistors, blue-light emitting, piezoelectric, and short wavelength laser diodes with low thresholds in the UV light-emitting diodes [8–10].

ZnO plays a significant role in the development of terahertz quantum cascade lasers (QCLs) due to its wide bandgap, which allows it to operate efficiently at high frequencies. High power terahertz sources which operate at room temperature show interest for a variety of uses, including reliable connectivity telecommunication, non-invasive medical imaging, and the detection of explosive materials [11]. This makes ZnO ideal for terahertz radiation generation, offering high electron mobility and effective electron transport. In hybrid LEDs, ZnO is used as a transparent conductive layer, improving charge injection and light emission efficiency. Its optical properties, such as high transparency and durability, enhance the overall performance and energy efficiency of LED devices, making ZnO an important material for advancing optoelectronics [12]. Therefore, our goal is to better understand how Sb segregation affects the atomic and electronic structure of a ZnO model tilt boundary system.

Pure ZnO is well known for exhibiting *n*-type conductivity characteristics. It took place as a result of intrinsic donors like H incorporation [6], zinc interstitials (Zn_i), and oxygen vacancies resulting in a departure from stoichiometry. Alternatively, a consequence of levels of dopants, *p*-type conduction in ZnO is generally characterized by low hole concentration, instability, and relatively low hole mobility. In general, the

ZnO doped with specific elements the electrical, optical, and magnetic properties can be manipulated. However, formation of the high-quality *p*-type ZnO is complicated due to factors such as deep acceptor levels, low solubility of acceptor dopants, and a strong self-compensating effect caused by native defects like zinc interstitials (Zn_i), oxygen vacancies (V_O), and hydrogen incorporation [13, 14]. Even though theoretical calculations demonstrated that *p*-type ZnO could be created by substituting the O by the group V elements (like N, P, As, and Sb), but the experimental research on *p*-type doped ZnO have demonstrated that it is highly difficult to produce low-resistivity *p*-type ZnO [15].

At present, a great deal of research has been performed on the behavior of *p*-type ZnO in an attempt to comprehend the successful fabrication of *p*-type ZnO materials [16]. N-In co-doped *p*-type ZnO, N-Al co-doped *p*-type ZnO [17], Cu doped *p*-type ZnO [18], and some homojunctions [19–21] have been successfully fabricated, according to some groups. Group V elements, such as N and P [22, 23], have been utilized to create the *p*-type ZnO. Among other elements, there have been a few reports of *p*-type ZnO for As or Sb [24]. Nevertheless, the deep acceptor levels and significant size mismatching of Sb-doped ZnO make them highly mysterious.

In the past few years, it has been proposed that group V dopant Sb may correlate to relatively shallow acceptor levels in ZnO according to first principle studies. This was based on the theory that a Sb atom could take the place of a Zn atom and at the same timeframe create two Zn vacancies in a process that involves five-fold coordination [25]. Based on this theory, Xiu et al. reported that hall effect measurements for ZnO films using molecular beam epitaxy showed *p*-type conduction [26]. Mandalapu et al. demonstrated the initially Sb doped *p*-ZnO/*n*-Si device performance [27]. They pointed out that Sb is a promising element for *p*-type doping in ZnO thin films for UV optoelectronic applications using Molecular Beam Epitaxy (MBE).

As far as we know, little study has been done on *p*-type ZnO, both theoretically and experimentally. Thus, in order to analyze the impact of Sb on the *p*-type ZnO doping, we must employ the first principles approach. Meanwhile, Sb is proposed as a better candidate to realize *p*-type ZnO with higher carrier concentration [28, 29], even though the atomic radius is much larger. Sb-doped ZnO material research is still ongoing currently this moment [30–33]. One effective way to achieve *p*-type conductivity in ZnO could be to increase the concentration of Sb [30]. However, it is appeared that an overly high Sb doping level hinders effective *p*-type doping because, as the mole ratio of Sb precursor to Zn precursor increases, the conductivity type of Sb doped ZnO shifts from *p*-type to *n*-type [32]. Consequently, Sb doped ZnO nanostructures should be a good option for a UV photodetector at the nanoscale [33] and ought to be a promising candidate for nanoscale UV photodetector.

2. COMPUTATIONAL DETAILS

In this study, the first principles calculations were performed using the Cambridge Serial Total Energy Package (CASTEP) code [34] for calculating the lattice parameters, electronic band structure, Density of States (DOS) and optical properties of Sb-doped ZnO. Perdew–Burke–Ernzerhof (PBE) and the Generalized Gradient Approximation (GGA) have been employed as exchange-correlation functionals on a framework of Density Functional Theory (DFT) [35]. For Zn, O, and Sb atoms, ultrasoft pseudopotentials have been employed to simulate the ion-electron coupling. The consequences of the spin-orbit interaction has been disregarded. For Zn, O, and Sb, the valence electron configurations were calculated to be $3d^{10}4s^2$, $2s^22p^4$, and $4d^{10}5s^25p^3$, respectively.

ZnO is a $C_{6v\text{-}4}$ symmetry system possessing a hexagonal-wurtzite structure and belongs to a member of the $P6_3mc$ [36] space group. The unit cell is made up of two Zn two O as the role of cations and anions, respectively. Consequently, a sequence of Zn-O double layers stacked along the *c*-axis or (001) directions can be used to describe the ZnO crystal. The second nearest neighbor distances are $a = 3.25$ Å, $c = 5.21$ Å, $\alpha = \beta = 90°$, $\gamma = 120°$ [37–40]. It is observed that, the bond length of pure ZnO is 1.99 Å along the *c* axis, 1.97 Å along the other axis, and the c/a ratio is 1.602 [41]. To compute all the parameters of pure and Sb = 6.25 (on Zn-site) doped ZnO $2 \times 2 \times 2$ supercells, the Brillouin Zone (BZ) was sampled using the $4 \times 4 \times 2$ Monkhorst and Pack [42] grid and the plane-wave cut-off energy of 400 eV. Reciprocal space is used for all mathematical operations. The maximum force was set to 0.03 eV/Å, the maximum stress taken at 0.05 GPa, and the overall energy at 5×10^{-5} eV/atom, with convergence limits specified for geometry optimization. We take into account a cell larger than the fundamental unit in order to analyze the fractional Sb substitution. As a result, we formulated the supercell $2 \times 2 \times 2$ supercell of pure ZnO consists of 32 atoms (16 atoms represent Zn and 16 atoms represent O-atoms), as seen in Figs. 1a and 1b.

3. RESULTS AND DISCUSSION

3.1. Geometry Optimization and Structural Properties

The ZnO is a wurtzite hexagonal crystal structure having space group $P6_3mc$ with Zn and O-atomic planes stacked alternately along the direction of *c*-axis illustrated in Fig. 1. First, in order to investigate how impurities influenced the stability of the structure during the calculation, the structure of pure and

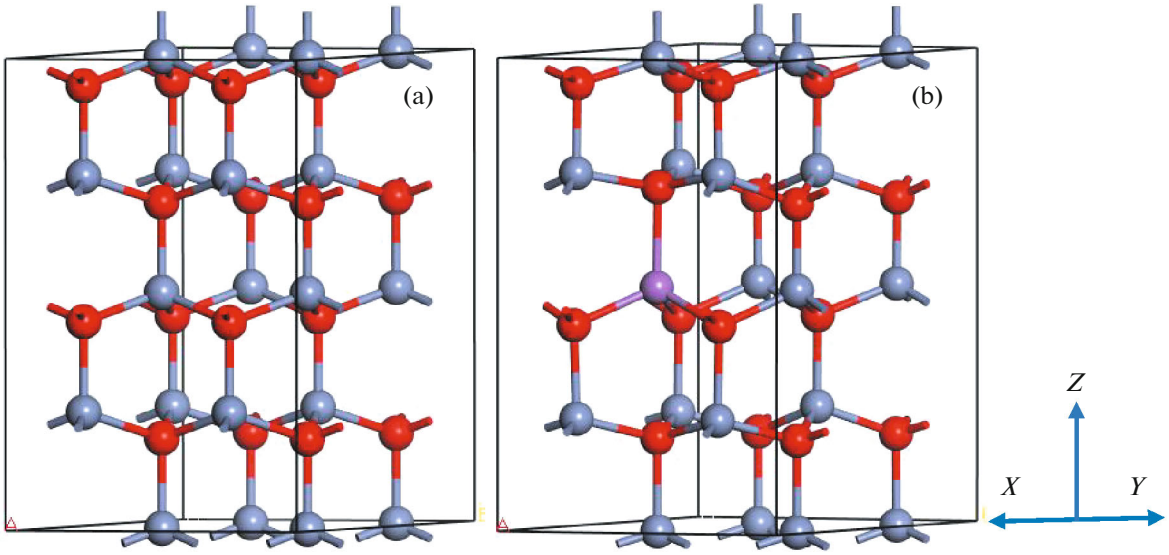

Fig. 1. Optimized structures of (a) pure, (b) Sb = 6.25% doped ZnO 2 × 2 × 2 supercells.

6.25% Sn doped ZnO 2 × 2 × 2 supercells were optimized. Following geometry optimization, the band structure and DOS were calculated. Table 1 lists the computed results for structural and electronic analysis, which are consistent with the theoretical results [15, 43–46] and demonstrate the reliability of the computational methods. The obtained lattice constants are observed to be a bit larger than those for pure and Sb doped ZnO [37, 45, 47, 48]. It is noteworthy that, these assumptions differ simply by between one and five percent from the experimental values (a = 3.25 Å, c = 5.21 Å) [37–40] which demonstrates that our calculations are reasonable.

The calculated bond length between Zn and O (Zn-O bond length) along the c-axis for pure and Sb doped ZnO are obtained 2.202 and 2.317 Å, respectively, which are marginally greater than that of the bulk ZnO 1.991 Å [45] and also become concurrent with the theoretical and experimental results as represented in Table 1 [43, 49]. The electronic configuration of Sb is $4d^{10}\ 5s^2\ 5p^3$. The observed distortion in the ZnO monolayer upon substituting Zn^{2+} with Sb^{3+} atoms may be attributed to the larger ionic radius of the Sb^{3+} ion (0.76 Å) compared to the Zn^{2+} ion (0.74 Å). Despite this size difference, the incorporation of Sb leads to notable distortions in the structure of the ZnO monolayer. Consequently, the grain size tends to increase, suggesting that Sb has a significant influence on the grain growth of ZnO [50]. However, this increase in grain size can lead to a reduction in the material's mechanical strength and crystal hardening properties [43]. Moreover, the relaxed hexagonal structures (shown in Figs. 1a and 1b) indicate that the Zn-O bond length remains uniform, which is a result

Table 1. Structural and electronic parameters of pure ZnO and $Zn_{93.75}Sb_{6.25}O$ 2 × 2 × 2 supercells after geometry optimization

Sample's name	Lattice constants (Å)		Deviation (%)	Volume (Å^3)	c/a	Band gap, E_g (eV)	Bond length (calculated), Å	
ZnO	a	3.298[a], 3.278[b], 3.298[c], 3.295[d]	1.47	49.914	1.606	0.730	Zn–O	2.022[a], 1.985[e], 1.890[g], 1.99[h], 1.98[h]
	c	5.299[a], 5.295[b], 5.286[c], 5.290[d]	1.53					
$Zn_{93.75}Sb_{6.25}O$	a	3.319[a], 3.267[e], 3.276[f]	2.12	52.174	1.648	0.178	Zn–O	2.317[a], 2.477[e], 1.980[g]
	c	5.469[a], 5.292[e], 5.288[f]	4.97					

[a] Present work, [b] [52], [c] [53], [d] [34], [e] [45], [f] [44], [g] [51], [h] [54].

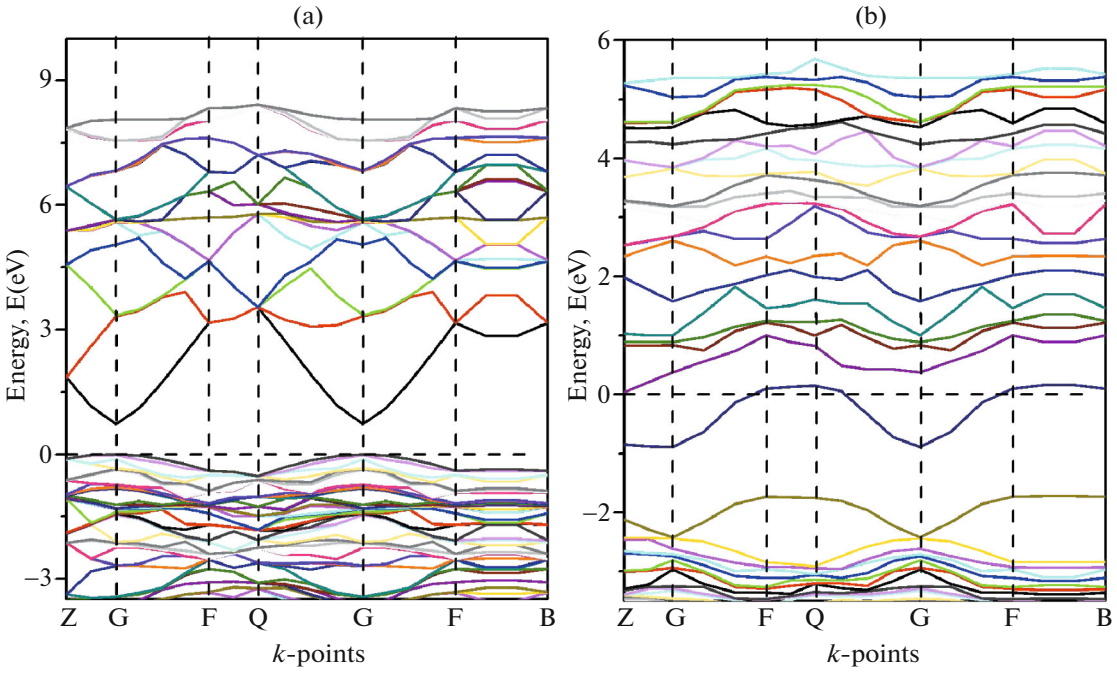

Fig. 2. Calculated band structures of (a) pure, (b) Sb = 6.25% doped ZnO 2 × 2 × 2 supercells.

of the high symmetry within the geometry. Even with the substitution of Zn by the larger Sb atom, the 2D configuration of the ZnO monolayer is largely preserved, with only minor distortions observed [51].

3.2. Band Structure and Density of States (DOS)

To gain insights into the orbital contributions in both pure and Sb-doped ZnO monolayers, we conducted a detailed study of the electronic structure. This analysis included the total density of states (TDOS) and partial density of states (PDOS), using the generalized gradient approximation (GGA) functional. Notably, our calculations were performed without incorporating spin-orbit interactions, allowing us to focus on the intrinsic electronic characteristics of the system. Figures 2a and 2b represent the electronic band structure along the high-symmetry paths Z-G-F-Q-G-F-B in the first Brillouin zone. To clearly distinguish between the conduction and valence bands relative to the Fermi level, we set the Fermi level (EF) to zero in our analysis. From Fig. 2a, it is evident that ZnO behaves as a direct band gap semiconductor, with the band gap energy calculated to be approximately 0.73 eV. This value is in good agreement with previously reported results obtained through density functional theory (DFT) calculations. In this structure, both the conduction band minimum (CBM) and the valence band maximum (VBM) are located at the same *k*-point along the (G-G) path in the Brillouin zone, confirming the direct band gap nature of ZnO [37, 43, 47, 52–63].

However, this calculated band gap is considerably smaller than the experimentally observed band gap of 3.37 eV for ZnO [2, 64]. This discrepancy is a common issue associated with traditional DFT calculations, where the electronic band gaps of semiconductors are typically underestimated. This is due to the fact that DFT often neglects the electron-electron correlation effects in the excited states, which are crucial for accurately predicting the electronic properties of materials, particularly their band gaps [37, 47, 52, 55–60, 65–68].

Furthermore, our analysis reveals that the Zn-3*d* and O-2*p* orbitals primarily contribute to the formation of the valence band in ZnO. These orbitals dominate the bonding and electronic states in the valence region. On the other hand, the conduction band is mainly composed of the Zn-3*s* and O-2*p* states. These findings highlight the crucial role of both zinc and oxygen orbitals in determining the electronic properties of ZnO, particularly in the formation of its band structure.

Figure 2b represents the effect of Sb concentration on the band structure. The Zn-3*d* and Sb-5*p* states predominate in the conduction band of Sb doped ZnO systems. As the region of occupied states increases, these donor states close to the Fermi level improve conductivity and delocalize spectra with *n*-type carrier concentration [51]. Figure 2b provides a clear indication of the characteristics of a typical *p*-type degenerate semiconductor, where the Fermi level shifts downward into the valence band. This downward shifting in the Fermi level is a defining trait of *p*-type materials. Specifically, when Zn atoms, that has the electron

configuration $4s^2$, are substituted with Sb atoms which possess electron configuration $5s^25p^3$, the carrier concentration of electrons is reduced. This reduction in the electron concentration results in the Fermi level being pushed further into the valence band, as shown in the figure [69].

For the specific case of Sb-doped ZnO with a doping concentration of 6.25%, the band gap is found to decrease significantly to 0.178 eV, as depicted in Fig. 2b. This is a notable reduction compared to the band gap of pure ZnO, as shown in Fig. 2a and summarized in Table 1. The decrease in the band gap is attributed to the formation of an impurity energy level, often referred to as the acceptor level, which appears near the top of the valence band due to the introduction of Sb atoms. This acceptor level causes the Fermi level to shift downward by approximately 0.148 eV. The appearance of this acceptor level facilitates the movement of electrons from the valence band to the impurity energy levels, thus increasing the carrier concentration in the valence band [69]. This result is consistent with previous findings in the literature, where similar trends have been observed for Sb doped ZnO and other materials [1, 52, 65–68, 70–75].

The key mechanism behind the reduction of the band gap and the shift in the Fermi level is the increased availability of acceptor levels introduced by the Sb dopants. These levels allow electrons to be easily excited from the valence band to the impurity levels, which increases the concentration of hole carriers in the valence band. As shown in Fig. 2b, this process effectively introduces a deep acceptor level within the energy gap of Sb doped ZnO at a concentration of 6.25%. The presence of this deep acceptor level enhances the stability of the *p*-type ZnO system, as the increased hole concentration improves the overall conductivity and performance of the material. This result highlights the important role that Sb doping plays in not only improving the *p*-type conductivity of ZnO but also enhancing the material's stability and overall quality. Therefore, Sb doped ZnO can be considered a more stable and high-quality material for *p*-type semiconductor applications, as it promotes a more efficient and reliable *p*-type ZnO system [1, 37, 47, 52, 55–60, 63, 65–68, 74–82].

The electronic band structures of pure and 6.25% Sb ZnO are effectively depicted through the (TDOS) and (PDOS) shown in Figs. 3a and 3b, respectively. These figures provide a detailed view of the contributions from different atomic orbitals to the electronic structure. In Fig. 3a, the valence bands of ZnO are clearly divided into two distinct regions, each dominated by different electronic interactions. The lower portion of the valence band, spanning from −6.20 to −4.66 eV, is primarily formed by the *d*-*p* hybridization of Zn-3*d* and O-2*p* orbitals. This hybridization creates a bonding interaction between the Zn and O atoms, significantly influencing the electronic states in this energy range. Although, the Zn-4*s* orbitals also contribute to this lower valence band, their influence is relatively minor compared to the strong interaction between Zn-3*d* and O-2*p* states. This hybridized region plays a critical role in defining the material's electronic characteristics, as it governs the bonding interactions and the overall stability of the valence band.

Above −4.66 eV, the electronic states in the upper valence bands are predominantly derived from O-2*p* orbitals, indicating a stronger oxygen character in this region of the band structure. However, there are still some minor contributions from Zn-3*d* and Zn-4*s* states, although their influence is considerably weaker than that of the O-2*p* orbitals. This shift in the dominant orbital character above −4.66 eV suggests that the upper valence bands are more influenced by the oxygen atoms, which can affect the material's electronic properties, such as its conductivity and optical behavior.

The detailed analysis of these valence bands reveals the intricate nature of the bonding and electronic interactions in ZnO. The division between the lower and upper valence bands, based on the contributions from different atomic orbitals, highlights the key role played by both Zn and O atoms in the material's electronic structure. This information is crucial for understanding the fundamental properties of ZnO, especially when considering the impact of doping Sb doping on modifying these electronic characteristics.

Additionally, it is seen from Fig. 3a, the O-2*s* states around −17 eV are excluded from the analysis due to their negligible interaction with other valence bands. These O-2*s* states are predominantly derived from the oxygen atoms and contribute only weakly to the overall electronic structure, with a slight influence from the Zn-4*s* and Zn-3*d* orbitals. This suggests that the O-2*s* orbitals do not significantly participate in the bonding interactions that govern the material's primary electronic properties.

On the other hand, the conduction band of ZnO is mainly composed of Zn-4*s* states, with only a small contribution from Zn-3*d* and O-2*p* states. The Zn-4*s* states play a pivotal role in determining the conductive behavior of ZnO, as these orbitals are involved in charge transfer processes. Specifically, electrons are transferred from the Zn-4*s* levels to the O-2*p* levels, a process that contributes to the material's electronic conductivity. This charge transfer leads to a shift in the center of gravity of the local density of states (LDOS) at the oxygen sites, causing it to move toward lower energy levels [41]. This shift indicates that the Zn-4*s* states are directly influencing the electronic properties of the material, enhancing its conductivity by facilitating charge transfer.

The strong contribution of Zn-4*s* states to the conduction band and their role in charge transfer point to the characteristics of ZnO as a mixed bond metal

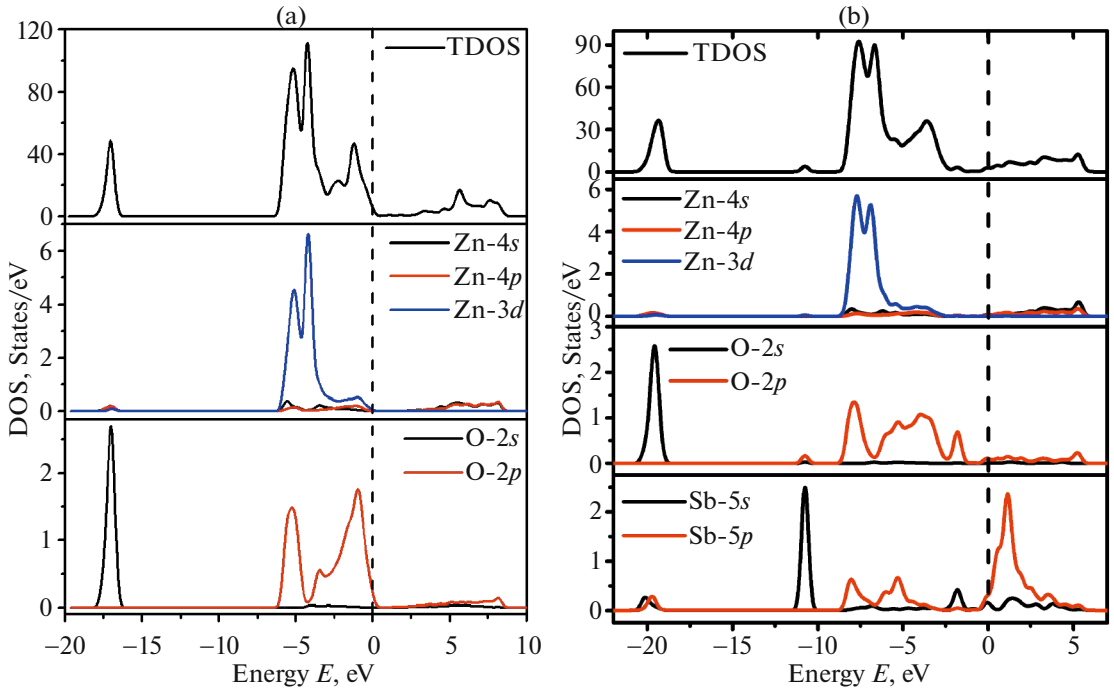

Fig. 3. Total and partial density of states of (a) pure, (b) Sb = 6.25% doped ZnO 2 × 2 × 2 supercells.

oxide semiconductor. In this type of material, the ionic bonding between Zn and O atoms is significantly stronger than the covalent bonding, which is a defining feature of the electronic structure. The dominance of ionic bonding in ZnO impacts several key properties of the material, including its electrical conductivity, stability, and optical characteristics. These findings reinforce the idea that ZnO, with its ionic bonding nature, exhibits semiconductor behavior driven by the interaction between Zn-4*s* and O-2*p* states.

Moreover, the results presented in this study are consistent with previous theoretical work performed by first-principles calculations, that have been used to characterize the electronic structure of pure ZnO. These studies have also observed similar trends in the electronic band structure and the role of Zn-4*s* states in the conduction process, further supporting the interpretation that ZnO exhibits strong ionic bonding and mixed bonding characteristics. The alignment of these findings with prior reports underscores the validity of the conclusions drawn from this analysis and strengthens the understanding the behavior of ZnO as a mixed bond metal oxide semiconductor material [1, 37, 43, 47, 52, 55–59, 61–63, 65–68].

Figure 3b illustrates the total and partial DOS for Sb doped ZnO, providing a deeper understanding of the material's electronic structure and *p*-type characteristics. In Sb doped ZnO, the *p*-type behavior is driven by an excess of holes located at the top of the valence band (VB). This results in a downward shift of the Fermi level into the valence band, signifying the presence of acceptor states that contribute to hole formation and *p*-type conductivity. Specifically, when Sb atoms replace Zn atoms in the ZnO lattice, they introduce new electronic states that alter the material's electronic structure.

For Sb doping at the Zn site, the DOS data in Fig. 3b show that the holes within the valence band create an acceptor level located near the middle of the band gap. This acceptor level is characterized by localization due to repulsive interactions between the narrow Sb impurity states and the surrounding electronic states in the lattice. The presence of this localized acceptor level plays a key role in the formation of holes that contribute to *p*-type nature.

When Sb is positioned at the Zn interstitial (Zn_i) sites, the partial DOS reveals the formation of additional peaks near the Fermi level, highlighting the impact of Sb doping on the electronic structure of ZnO. The Sb-5*s* states contribute to a distinct peak located at the bottom of the lower valence band, around −10 eV. Additionally, the Sb-5*p* states generate two other peaks, one at approximately −8 eV and another at −5 eV, indicating the presence of impurity states in the lower to mid-energy range. A prominent peak attributed to the Sb-5*p* states appears above the Fermi level, further influencing the overall electronic structure of the material. This peak is crucial as it reflects the energy levels that facilitate charge transfer, promoting *p*-type conductivity.

The Sb doping induced shifts in the DOS result in the movement of electronic states towards lower

energy levels, leading to a reduction in the optical band gap. This narrowing of the band gap is primarily due to the contribution of Sb-5*p* states, which occupy energy levels near the Fermi level and introduce new states within the band gap. These states provide additional pathways for electron excitation, lowering the energy required for electronic transitions and reducing the optical band gap.

Moreover, the majority of the holes in Sb doped ZnO are generated around the top of the valence band. This is consistent with the expected behavior of *p*-type semiconductors, where holes at the top of the VB act as charge carriers. However, a self-compensation effect arises due to the position of the acceptor level induced by Sb impurities on the Zn interstitial sites. The acceptor level appears relatively close to the Fermi energy, which leads to a situation where the introduction of holes is somewhat counterbalanced by the presence of these acceptor levels. This self-compensation effect is a significant challenge in optimizing the *p*-type properties of Sb doped ZnO. It complicates the formation of stable *p*-type conductivity, as the acceptor states that generate holes also reduce the overall carrier concentration.

The findings suggest that Sb doping in ZnO causes the Fermi level to shift downward into the valence band, significantly altering the bottom of the valence band. The impurity states introduced by Sb in the band gap act as acceptor levels, reinforcing the *p*-type character of the material. However, the self-compensation effect, particularly when Sb occupies interstitial sites, presents a major obstacle in achieving high quality *p*-type ZnO. These results underscore the complexity of achieving high quality *p*-type ZnO materials and highlight the delicate balance between acceptor and donor states, which affects the material's overall conductivity and electronic properties [41].

3.3. Optical Properties

The investigation of the optical properties is a crucial aspect of this research, as it plays a key role in enhancing the performance of ZnO based optoelectronic devices. Specifically, improving the quality of *p*-type ZnO materials and reducing the optical band gap could significantly contribute to the development of high performance electronic devices. These advancements are essential for optimizing the functionality of ZnO in various optoelectronic applications, as reported in previous studies [83, 84].

To gain a comprehensive understanding of the optical behavior, this study focuses on several key optical constants, including the real and imaginary parts of the dielectric constants, $\varepsilon_r(\omega)$ and $\varepsilon_i(\omega)$, respectively, the refractive index $n(\omega)$, the absorption coefficient $\alpha(\omega)$, and photoconductivity $\sigma(\omega)$. These properties were thoroughly investigated through first principles calculations, using the Density Functional Theory (DFT) framework. The generalized gradient approximation (GGA) and Perdew–Burke–Ernzerhof (PBE) functional were employed as exchange-correlation functionals to model the electronic structure and optical responses of the material. These computational methods allow for an accurate and detailed prediction of the material's optical characteristics, which are essential for optimizing ZnO based devices.

3.4. Dielectric Constant

Optical properties are very crucial in comprehending the nature of materials and provide valuable insights for optoelectronic applications. Generally, the complex dielectric function $\varepsilon_i(\omega)$, which governs how radiation propagates through a medium and characterizes the linear response of electromagnetic radiation, can be used to illustrate the optical properties of the material of interest which is given by the following relation (1),

$$\varepsilon(\omega) = \varepsilon_r(\omega) + i\varepsilon_i(\omega), \quad (1)$$

where $\varepsilon_r(\omega)$ and $\varepsilon_i(\omega)$ represent the real and imaginary components of the dielectric functions, respectively. The $\varepsilon_r(\omega)$ of pure and Sb doped ZnO are depicted in Fig. 4. At photon energy 0.0 eV, the values of $\varepsilon_r(0)$ for pure and 6.25% Sb doped ZnO are found to be 3.96 and 28.58, respectively. It is clear that, for Sb-doped ZnO structures, the line shape of the real part of the dielectric function, $\varepsilon_r(\omega)$, remains nearly identical in the high energy range. However, its influence of Sb enrichment is most noticeable in the low energy region, significantly altering the behavior of $\varepsilon_r(\omega)$ [57]. This suggests that the doping with Sb has a more noticeable effect on the electronic properties of ZnO at lower energies, while the higher-energy response remains largely unchanged. Consequently, after Sb doping, the static dielectric constant is increased. ZnO $\varepsilon_r(\omega)$ is not significantly affected by the defect at low dopant concentrations of Sb [57]. The increased value of $\varepsilon_r(0)$ observed for Sb doping suggests a narrowing of the band gap. This observation is further supported by the results from the current electronic band structure calculations, which confirm that Sb doping has a significant effect on reducing the band gap. These findings indicate that the introduction of Sb into the ZnO structure alters the electronic properties, leading to a smaller energy gap between the conduction and valence bands. It is taken into account, when photon energy increases, the value of $\varepsilon_r(\omega)$ sharply drops. About photon energy 1.30 eV Sb doped ZnO exhibits a valley-like shape that gradually increases to approximately 4.10 eV photon energy. At 9.96 and 9.38 eV photon energies, respectively, the first roots of $\varepsilon_r(\omega)$ for pure and Sb = 6.25% doped ZnO are found. Likewise, the respective second roots found at 13.84 and 13.73 eV. The second roots of the dielectric function, $\varepsilon_r(\omega)$, correspond to the plasma energy, which is the

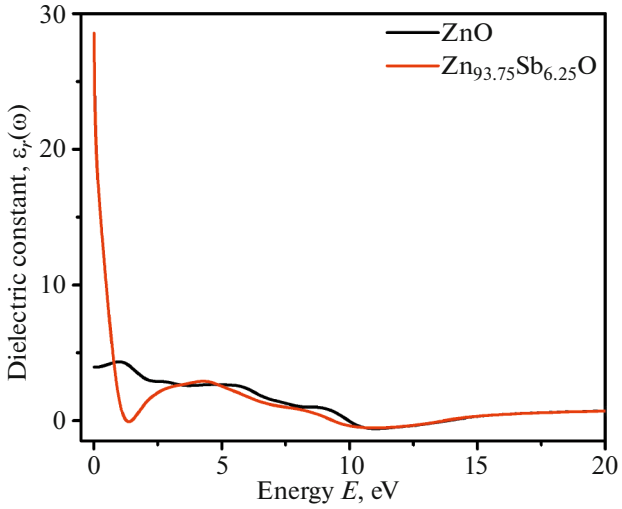

Fig. 4. Real dielectric constant of pure and Sb doped ZnO 2 × 2 × 2 supercells.

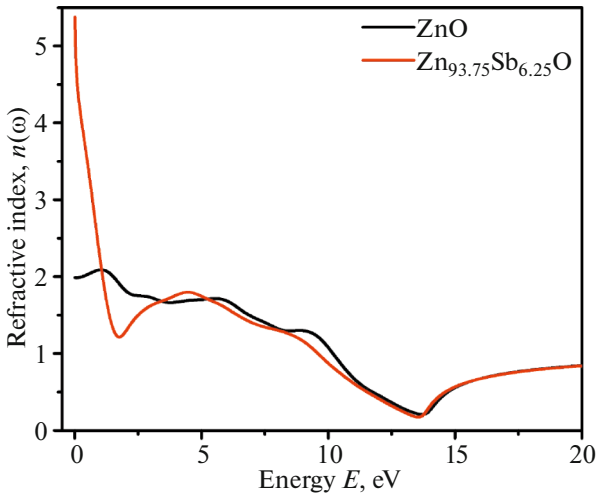

Fig. 5. Refractive index of pure and Sb doped ZnO 2 × 2 × 2 supercells.

specific energy at which $\varepsilon_r(\omega)$ transitions to a negative value. For the samples under investigation, the plasma energies were determined to be 13.84 and 13.73 eV, respectively. This finding indicates the energy threshold at which free carriers in the material begin to contribute to the dielectric response. In addition to the plasma energy behavior, an additional optical transition peak was observed at a photon energy of 4.35 eV. This peak can be attributed to the hybridization of impurity states, where the O-2*p* and Sb-5*p* states (specifically the holes in these states) interact with the Zn-4*s* states. Such hybridization leads to a distinct optical feature in the dielectric function. The estimated values for the real dielectric function obtained in this study are in excellent agreement with those reported in the literature, reinforcing the reliability of the findings [1, 37, 47, 53, 55–59, 69, 85–94].

3.5. Refractive Index

The changes in light waves brought about by interactions with materials are described by the refractive index, $n(\omega)$. This is typically very useful for nonmagnetic materials in connecting a material's dielectric characteristics to its optical characteristics at any specific frequency of interest. Precisely, $n(\omega)$ is dependent on the wavelength of the light and it also depends on the dispersion of the light. The refractive index, $n(\omega)$, of the pure and Sb doped ZnO supercells have been shown in Fig. 5. For every sample, the refractive index exhibits a well dispersive nature. Its maximum value is achieved at a particular energy, representing the significant polarization induced at that particular energy. The value of $n(\omega)$ lowers with increasing photon energy attribute after reaching its maximum due to varying loss mechanism participation [95]. They are similar that of dielectric constants which can be obtained by the root of the dielectric constants [96]:

$$n(\omega) = \sqrt{\varepsilon(\omega)}. \quad (2)$$

For pure and Sb = 6.25% doped ZnO, our calculated static refractive index $n(0)$ is ~1.99 and 5.38, respectively. The respective maximum values of $n(\omega)$ of pure and Sb = 6.25% doped are 2.10 and 5.38 obtained at energy 1.04 and 0.0 eV. It is found that as photon energy increases, $n(\omega)$ decreases. Notably, Sb-doped ZnO exhibits a high refractive index. From Fig. 5 the refractive indices of pure and Sb-doped ZnO are appeared to be decrease below unity at 10.0 eV. Consequently, after 10.0 eV, both pure and Sb-doped ZnO exhibit superluminal behavior. The phenomenon known as superluminal wave propagation, which occurs when electromagnetic waves travel faster in vacuum than light speed, is generally mentioned [94]. The obtained outcomes closely match the outcomes published in previous results [94].

3.6. Absorption

Figure 6 depicted the absorption coefficient, $\alpha(\omega)$, of pure and 6.25% Sb doped ZnO. The presence of a peak near the band gap value indicates the nature of direct optical transitions. This height of the peak goes up as Sb doping increases and shifts toward a lower energy to reflect the band gap narrowing. The intensity of this peak is reduced by Sb doping; this may be due to well incorporation of Sb in Zn site and in agreement with previous findings [39, 97]. The prominent large peak in the spectra is located at 10.55 eV. It has been noticed that in the UV region, $\alpha(\omega)$ increases. By taking absorption into account, the computed $\alpha(\omega)$ values agree fairly well with findings from previous studies [92, 97, 98]. The absorption $\alpha(\omega)$ spectra for

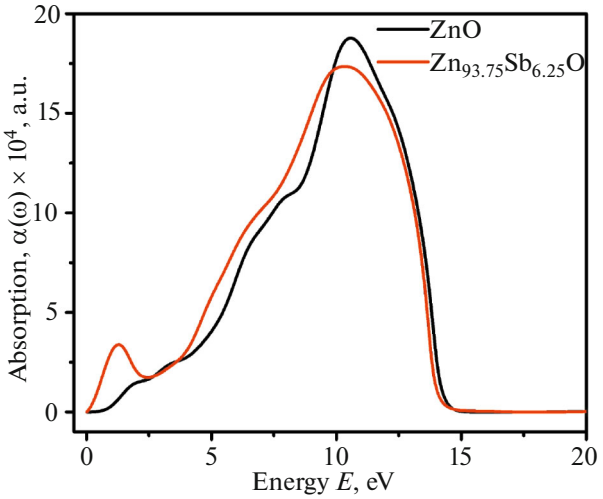

Fig. 6. Absorption co-efficient of pure and Sb doped ZnO 2 × 2 × 2 supercells.

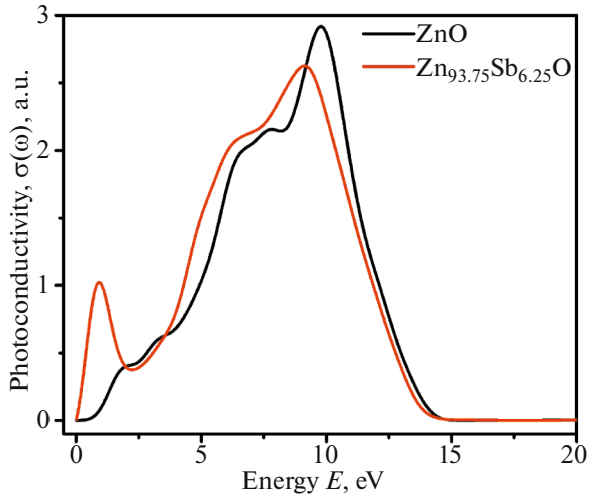

Fig. 7. Photoconductivity of pure and Sb doped ZnO 2 × 2 × 2 supercells.

Sb doped ZnO supercells are observed to range between 3 to 11 eV in the UV spectrum, indicating that these materials can effectively absorb incident photon energy within this energy range, as shown in Fig. 6. Thus, the materials may find use in electronic and optoelectronic devices as effective absorbers of incident energy falling within this energy range.

Furthermore, a notable observation is that when the incident photon energy surpasses 11 eV, the absorption coefficient, $\alpha(\omega)$, for both pure and Sb doped ZnO undergoes a sharp decrease. This behavior suggests that the material becomes optically transparent beyond this photon energy, meaning it no longer absorbs light in this range. The decline in $\alpha(\omega)$ marks a transition to a state where the electronic properties of materials are dominated by collective oscillations of free charge carriers, which is a characteristic behavior observed at the plasma frequency. At this energy, the material exhibits plasmonic effects, where the free carriers, such as electrons, oscillate collectively in response to electromagnetic fields. This phenomenon signifies the onset of a plasma like regime, further confirming the material's transition to transparency and the observation of plasmon energy, a key feature associated with the interaction of light and free carriers in the material.

3.7. Photoconductivity

The optical conductivity, $\sigma(\omega)$, for both pure and 6.25% Sb doped ZnO is presented in Fig. 7. Apart from the typical electron-hole pair generation, the Sb doped ZnO shows a noticeable peak at 0.90 eV. This peak is notable for shifting to lower energies with Sb doping, which is the key feature of the narrowing of the material's band gap. This behavior suggests that Sb doping influences the electronic structure of ZnO, altering its optical properties. The peak near the band gap in Sb doped ZnO is likely due to optical transitions between the Sb-5*p* states in the upper valence band and the O-2*p* states in the lower valence band. These transitions involve the hybridization of the impurity states with the host ZnO states, which can modify the electronic states near the band edge. Additionally, a higher energy peak appears above 1.0 eV, which can be attributed to optical transitions from the valence band to deeper impurity band states within the material. These impurity bands are formed due to the introduction of Sb into the ZnO lattice and represent states that lie below the conduction band but above the valence band.

Another important observation is that, the optical conductivity spectrum of Sb doped ZnO lies below that of pure ZnO across the measured energy range. This decrease in optical conductivity suggests that the doping process introduces a higher concentration of hole carriers in the valence band, which likely increases the overall conductivity but reduces the material's ability to absorb photons in the optical region. The presence of additional hole carriers due to Sb doping indicates the formation of a *p*-type ZnO, which is a key characteristic that can be leveraged for certain electronic and optoelectronic applications, such as diodes, transistors, and light emitting devices.

These findings are consistent with previous research on Sb doped ZnO and support the potential of this material for use in a variety of electronic and optoelectronic devices, where *p*-type conduction is necessary for device functionality [1, 37, 47, 52, 53, 55–59, 65–69, 85–91]. The observed shift in optical conductivity and band gap narrowing also suggests that Sb doping can be fine-tuned to optimize the material's properties for specific applications.

4. CONCLUSIONS

Sb doped ZnO has been investigated using first principles calculations within the framework of Density Functional Theory (DFT), using Perdew–Burke–Ernzerhof (PBE) and the Generalized Gradient Approximation (GGA) as the exchange-correlation functional. This study provides strong evidence for the *p*-type conductivity of Sb doped ZnO. It demonstrates that, the Sb doping leads to a narrowing of the band gap, which is a key characteristic of *p*-type materials. Furthermore, the doping introduces acceptor impurity bands at the top of the valence band, which are responsible for the creation of hole carriers in the material. These acceptor states facilitate the movement of holes, thus contributing to the *p*-type conductivity observed in Sb doped ZnO. The presence of these impurity bands and the associated band gap narrowing confirm the successful induction of *p*-type behavior, making Sb doped ZnO a promising candidate for various electronic and optoelectronic applications. Sb concentrations are shown to increase grain size, which results in a loss in mechanical strength and crystallinity hardening. Importantly, doping of Sb and photoconductivity both play crucial roles in promoting the formation of *p*-type ZnO. The incorporation of Sb introduces acceptor states that facilitate hole conduction, while photoconductivity further enhances the material's ability to conduct under light exposure. Together, these factors contribute to the development of *p*-type ZnO, which is essential for a wide range of electronic and optoelectronic applications. Therefore, the findings of this study could significantly aid in the design, fabrication, and optimization of devices that rely on *p*-type ZnO, such as transistors, light emitting diodes, and solar cells.

ACKNOWLEDGMENTS

Authors are thankful to Department of Physics, Begum Rokeya University, Rangpur, Rangpur 5400, Bangladesh and Department of Physics, Uttara University, Holding 77, Beribadh Road, Turag, Uttara, Dhaka-1230, Bangladesh for their full support and providing Computer Lab facilities to investigate the study.

AUTHOR CONTRIBUTION

The study was designed by Mosfiqur Rahman and Md. Kamruzzaman, who also interpreted the data and authored the manuscript. Meanwhile, Md. Al Helal and Md. Nurul Huda Liton contributed to the theoretical aspects of the research, assisted in data analysis, and supported the writing of the manuscript. Together, their collaborative efforts led to the completion of this study and the development of the manuscript.

FUNDING

This work was supported by ongoing institutional funding. No additional grants to carry out or direct this particular research were obtained.

CONFLICT OF INTEREST

The authors of this work declare that they have no conflicts of interest.

REFERENCES

1. O. Lupan, L. Chow, L. K. Ono, B. R. Cuenya, G. Chai, H. Khallaf, S. Park, and A. Schulte, J. Phys. Chem. C **114**, 12401 (2010). https://doi.org/10.1021/jp910263n
2. D. G. Thomas, J. Phys. Chem. Solids **15**, 86 (1960). https://doi.org/10.1016/0022-3697(60)90104-9
3. J. M. Carlsson, B. Hellsing, H. S. Domingos, and P. D. Bristowe, J. Phys.: Condens. Matter **13**, 9937 (2001). https://doi.org/10.1088/0953-8984/13/44/309
4. S. J. Pearton, D. P. Norton, K. Ip, Y. W. Heo, and T. Steiner, J. Vac. Sci. Technol., B: Microelectron. Nanometer Struct.–Process., Meas., Phenom. **22**, 932 (2004). https://doi.org/10.1116/1.1714985
5. D. C. Look, Mater. Sci. Eng., B **80**, 383 (2001). https://doi.org/10.1016/s0921-5107(00)00604-8
6. Ch. G. Van de Walle, Phys. Rev. Lett. **85**, 1012 (2000). https://doi.org/10.1103/PhysRevLett.85.1012
7. D. C. Look, J. W. Hemsky, and J. R. Sizelove, Phys. Rev. Lett. **82**, 2552 (1999). https://doi.org/10.1103/physrevlett.82.2552
8. Z. K. Tang, G. K. L. Wong, P. Yu, M. Kawasaki, A. Ohtomo, H. Koinuma, and Y. Segawa, Appl. Phys. Lett. **72**, 3270 (1998). https://doi.org/10.1063/1.121620
9. Y. Chen, N. T. Tuan, Yu. Segawa, H.-J. Ko, S.-K. Hong, and T. Yao, Appl. Phys. Lett. **78**, 1469 (2001). https://doi.org/10.1063/1.1355665
10. L. Xiao and X. Yang, Russ. J. Phys. Chem. A **93**, 902 (2019). https://doi.org/10.1134/S0036024419050339
11. V. P. Sirkeli and H. L. Hartnagel, Opto-Electron. Rev. **27**, 119 (2019). https://doi.org/10.1016/j.opelre.2019.04.002
12. M. N. Rezaie, Sh. Mohammadnejad, and Sh. Ahadzadeh, Opt. Laser Technol. **138**, 106896 (2021). https://doi.org/10.1016/j.optlastec.2020.106896
13. A. Janotti and Ch. G. Van de Walle, Phys. Rev. B **76**, 165202 (2007). https://doi.org/10.1103/physrevb.76.165202
14. E.-C. Lee, Y.-S. Kim, Y.-G. Jin, and K. J. Chang, Phys. Rev. B **64**, 85120 (2001). https://doi.org/10.1103/physrevb.64.085120
15. F. H. Zhang, Z. Y. Zhang, W. H. Zhang, S. Q. Xue, J. N. Yun, and J. F. Yan, (IEEE, 2008). https://doi.org/10.1109/inec.2008.4585577

16. J. M. Bian, X. M. Li, X. D. Gao, W. D. Yu, and L. D. Chen, Appl. Phys. Lett. **84**, 541 (2004). https://doi.org/10.1063/1.1644331
17. J. G. Lu, Z. Z. Ye, F. Zhuge, Y. J. Zeng, B. H. Zhao, and L. P. Zhu, Appl. Phys. Lett. **85**, 3134 (2004). https://doi.org/10.1063/1.1803935
18. F. Ghahramanifard, A. Rouhollahi, and O. Fazlolahzadeh, Superlattices Microstruct. **114**, 1 (2018). https://doi.org/10.1016/j.spmi.2017.07.019
19. A. Tsukazaki, A. Ohtomo, T. Onuma, M. Ohtani, T. Makino, M. Sumiya, K. Ohtani, Sh. F. Chichibu, S. Fuke, Yu. Segawa, H. Ohno, H. Koinuma, and M. Kawasaki, Nat. Mater. **4**, 42 (2005). https://doi.org/10.1038/nmat1284
20. T. Aoki, Yo. Hatanaka, and D. C. Look, Appl. Phys. Lett. **76**, 3257 (2000). https://doi.org/10.1063/1.126599
21. Y. R. Ryu, W. J. Kim, and H. W. White, J. Cryst. Growth **219**, 419 (2000). https://doi.org/10.1016/s0022-0248(00)00731-4
22. D. C. Look, D. C. Reynolds, C. W. Litton, R. L. Jones, D. B. Eason, and G. Cantwell, Appl. Phys. Lett. **81**, 1830 (2002). https://doi.org/10.1063/1.1504875
23. K.-K. Kim, H.-S. Kim, D.-K. Hwang, J.-H. Lim, and S.-J. Park, Appl. Phys. Lett. **83**, 63 (2003). https://doi.org/10.1063/1.1591064
24. J. Z. Zhao, H. W. Liang, J. C. Sun, Q. J. Feng, J. M. Bian, Z. W. Zhao, H. Q. Zhang, L. Z. Hu, and G. T. Du, Electrochem. Solid-State Lett. **11**, H323 (2008). https://doi.org/10.1149/1.2980342
25. S. Limpijumnong, S. B. Zhang, S.-H. Wei, and C. H. Park, Phys. Rev. Lett. **92**, 155504 (2004). https://doi.org/10.1103/physrevlett.92.155504
26. F. X. Xiu, Z. Yang, L. J. Mandalapu, D. T. Zhao, J. L. Liu, and W. P. Beyermann, Appl. Phys. Lett. **87**, 152101 (2005). https://doi.org/10.1063/1.2089183
27. L. J. Mandalapu, F. X. Xiu, Z. Yang, D. T. Zhao, and J. L. Liu, Appl. Phys. Lett. **88**, 112108 (2006). https://doi.org/10.1063/1.2186516
28. U. Wahl, J. G. Correia, T. Mendonça, and S. Decoster, Appl. Phys. Lett. **94**, 261901 (2009). https://doi.org/10.1063/1.3159474
29. F. Wang, J.-H. Seo, D. Bayerl, J. Shi, H. Mi, Zh. Ma, D. Zhao, Yi. Shuai, W. Zhou, and X. Wang, Nanotechnology **22**, 225602 (2011). https://doi.org/10.1088/0957-4484/22/22/225602
30. H. P. Dang, Q. H. Luc, T. T. Nguyen, and T. Le, J. Alloys Compd. **776**, 276 (2011). https://doi.org/10.1016/j.jallcom.2018.10.272
31. C. H. Zang, J. F. Su, B. Wang, D. M. Zhang, and Y. S. Zhang, J. Lumin. **131**, 1817 (2011). https://doi.org/10.1016/j.jlumin.2011.03.040
32. H. Liang, Yu. Chen, X. Xia, Q. Feng, Ya. Liu, R. Shen, Yi. Luo, and G. Du, Thin Solid Films **589**, 199 (2015). https://doi.org/10.1016/j.tsf.2015.05.004
33. C. Luo, L.-P. Ho, F. Azad, W. Anwand, M. Butterling, A. Wagner, A. Kuznetsov, H. Zhu, Sh. Su, and F. C.-C. Ling, J. Appl. Phys. **123**, 161525 (2018). https://doi.org/10.1063/1.4997510
34. S. J. Clark, M. D. Segall, Ch. J. Pickard, P. J. Hasnip, M. I. J. Probert, K. Refson, and M. C. Payne, Z. Kristallogr. - Cryst. Mater. **220**, 567 (2005). https://doi.org/10.1524/zkri.220.5.567.65075
35. J. P. Perdew, K. Burke, and M. Ernzerhof, Phys. Rev. Lett. **77**, 3865 (1996). https://doi.org/10.1103/physrevlett.77.3865
36. R. Baghdad, B. Kharroubi, A. Abdiche, M. Bousmaha, M. A. Bezzerrouk, A. Zeinert, M. El Marssi, and K. Zellama, Superlattices Microstruct. **52**, 711 (2012). https://doi.org/10.1016/j.spmi.2012.06.023
37. M. A. Thomas, W. W. Sun, and J. B. Cui, J. Phys. Chem. C **116**, 6383 (2012). https://doi.org/10.1021/jp2107457
38. J. Lee, S. Cha, J. Kim, H. Nam, S. Lee, W. Ko, K. L. Wang, J. Park, and J. Hong, Adv. Mater. **23**, 4183 (2011). https://doi.org/10.1002/adma.201101376
39. Md. N. H. Liton, A. K. M. Farid Ul Islam, Md. Kamruzzaman, Md. K. R. Khan, Md. A. Helal, and Md. M. Rahman, Mater. Chem. Phys. **242**, 122463 (2020). https://doi.org/10.1016/j.matchemphys.2019.122463
40. S. C. Abrahams and J. L. Bernstein, Acta Crystallogr., Sect. B: Struct. Crystallogr. Cryst. Chem. **25**, 1233 (1969). https://doi.org/10.1107/s0567740869003876
41. Zh. Fu-Chun, Zh. Zhi-Yong, Zh. Wei-Hu, Ya. Jun-Feng, and Yu. Jiang-Ni, Chin. Phys. Lett. **25**, 3735 (2008). https://doi.org/10.1088/0256-307x/25/10/059
42. H. J. Monkhorst and J. D. Pack, Phys. Rev. B **13**, 5188 (1976). https://doi.org/10.1103/physrevb.13.5188
43. M. Rahman, M. Kamruzzaman, J. A. Zapien, R. Afrose, T. K. Anam, M. N. H. Liton, M. A. Helal, and M. K. R. Khan, Mater. Today Commun. **33**, 104278 (2022). https://doi.org/10.1016/j.mtcomm.2022.104278
44. V. Ribić, A. Rečnik, M. Komelj, A. Kokalj, Z. Branković, M. Zlatović, and G. Branković, Acta Mater. **199**, 633 (2020). https://doi.org/10.1016/j.actamat.2020.08.035
45. C.-Q. Luo, S.-C. Zhu, Ch. Xu, Sh. Zhou, C.-H. Lam, and F. C.-C. Ling, J. Magn. Magn. Mater. **529**, 167908 (2021). https://doi.org/10.1016/j.jmmm.2021.167908
46. X. Qu, Sh. Lü, L. Bai, Q. Meng, and D. Jia, Phys. B: Condens. Matter (Amsterdam, Neth.) **407**, 268 (2012). https://doi.org/10.1016/j.physb.2011.10.045
47. Q. Hou, Ch. Zhao, X. Jia, and Zh. Xu, Int. J. Mod. Phys. B **32**, 1850099 (2018). https://doi.org/10.1142/s0217979218500996
48. F. Decremps, F. Datchi, A. M. Saitta, A. Polian, S. Pascarelli, A. Di Cicco, J. P. Itié, and F. Baudelet, Phys. Rev. B **68**, 104101 (2003). https://doi.org/10.1103/physrevb.68.104101
49. C. Supatutkul, S. Pramchu, A. P. Jaroenjittichai, and Y. Laosiritaworn, J. Phys.: Conf. Ser. **901**, 012172 (2017). https://doi.org/10.1088/1742-6596/901/1/012172
50. M. Kamruzzaman, J. A. Zapien, R. Afrose, T. K. Anam, M. Rahman, M. N. H. Liton, M. A. Helal, M. K. R. Khan, and A. Ayotunde Emmanuel, Mater. Sci. Eng., B **273**,

115442 (2021).
https://doi.org/10.1016/j.mseb.2021.115442

51. S. Y. Wakhare and M. D. Deshpande, J. Mol. Graphics Modell. **101**, 107753 (2020).
https://doi.org/10.1016/j.jmgm.2020.107753
52. D. C. Look, G. M. Renlund, R. H. Burgener, and J. R. Sizelove, Appl. Phys. Lett. **85**, 5269 (2004).
https://doi.org/10.1063/1.1825615
53. M. Ardyanian and N. Sedigh, Bull. Mater. Sci. **37**, 1309 (2014).
https://doi.org/10.1007/s12034-014-0076-4
54. C. Supatutkul, S. Pramchu, A. P. Jaroenjittichai, and Y. Laosiritaworn, J. Phys.: Conf. Ser. **901**, 012172 (2017).
https://doi.org/10.1088/1742-6596/901/1/012172
55. S. M. Hosseini, I. A. Sarsari, P. Kameli, and H. Salamati, J. Alloys Compd. **640**, 408 (2015).
https://doi.org/10.1016/j.jallcom.2015.03.136
56. Ya. Yan, M. M. Al-Jassim, and S.-H. Wei, Appl. Phys. Lett. **89**, 181912 (2006).
https://doi.org/10.1063/1.2378404
57. Ya. Li, X. Zhao, and W. Fan, J. Phys. Chem. C **115**, 3552 (2011).
https://doi.org/10.1021/jp1098816
58. S. Masoumi, E. Nadimi, and F. Hossein-Babaei, Phys. Chem. Chem. Phys. **20**, 14688 (2018).
https://doi.org/10.1039/c8cp01578c
59. S. Khosravi-Gandomani, R. Yousefi, F. Jamali-Sheini, and N. M. Huang, Ceram. Int. **40**, 7957 (2014).
https://doi.org/10.1016/j.ceramint.2013.12.145
60. Z. Chun-Ying, W. Jing, and B. Yue-Lei, Chin. Phys. B **19**, 047101 (2010).
https://doi.org/10.1088/1674-1056/19/4/047101
61. H.-C. Wu, Y.-C. Peng, and T.-P. Shen, Materials **5**, 2088 (2012).
https://doi.org/10.3390/ma5112088
62. L. Li, W. Wang, H. Liu, X. Liu, Q. Song, and Sh. Ren, J. Phys. Chem. C **113**, 8460 (2009).
https://doi.org/10.1021/jp811507r
63. F.-W. Xie, P. Yang, P. Li, and L.-Q. Zhang, Opt. Commun. **285**, 2660 (2012).
https://doi.org/10.1016/j.optcom.2012.01.087
64. A. Ohtomo, M. Kawasaki, I. Ohkubo, H. Koinuma, T. Yasuda, and Y. Segawa, Appl. Phys. Lett. **75**, 980 (1999).
https://doi.org/10.1063/1.124573
65. T. K. Pathak, R. E. Kroon, and H. C. Swart, Vacuum **157**, 508 (2018).
https://doi.org/10.1016/j.vacuum.2018.09.020
66. M. Joseph, H. Tabata, H. Saeki, K. Ueda, and T. Kawai, Phys. B: Condens. Matter (Amsterdam, Neth.) **302–303**, 140 (2001).
https://doi.org/10.1016/s0921-4526(01)00419-7
67. F. X. Xiu, Z. Yang, L. J. Mandalapu, J. L. Liu, and W. P. Beyermann, Appl. Phys. Lett. **88**, 52106 (2006).
https://doi.org/10.1063/1.2170406
68. L. J. Mandalapu, F. X. Xiu, Z. Yang, D. T. Zhao, and J. L. Liu, Appl. Phys. Lett. **88**, 112108 (2006).
https://doi.org/10.1063/1.2186516
69. E.-C. Lee and K. J. Chang, Phys. Rev. B **70**, 115210 (2004).
https://doi.org/10.1103/physrevb.70.115210
70. A. Chelouche, T. Touam, M. Tazerout, D. Djouadi, and F. Boudjouan, J. Lumin. **188**, 331 (2017).
https://doi.org/10.1016/j.jlumin.2017.04.047
71. A. Chelouche, T. Touam, F. Boudjouan, D. Djouadi, R. Mahiou, A. Bouloufa, G. Chadeyron, and Z. Hadjoub, J. Mater. Sci.: Mater. Electron. **28**, 1546 (2017).
https://doi.org/10.1007/s10854-016-5694-8
72. F. Boudjouan, A. Chelouche, T. Touam, D. Djouadi, R. Mahiou, G. Chadeyron, A. Fischer, and A. Boudrioua, J. Mater. Sci.: Mater. Electron. **27**, 8040 (2016).
https://doi.org/10.1007/s10854-016-4800-2
73. T. Touam, F. Boudjouan, A. Chelouche, S. Khodja, M. Dehimi, D. Djouadi, J. Solard, A. Fischer, and A. Boudrioua, Optik **126**, 5548 (2015).
https://doi.org/10.1016/j.ijleo.2015.09.066
74. V. V. S. Kumar and D. Kanjilal, J. Chin. Adv. Mater. Soc. **2**, 199 (2014).
https://doi.org/10.1080/22243682.2014.937741
75. O. Volnianska, P. Boguslawski, J. Kaczkowski, P. Jakubas, A. Jezierski, and E. Kaminska, Phys. Rev. B **80**, 245212 (2009).
https://doi.org/10.1103/physrevb.80.245212
76. R. Deng, B. Yao, Y. F. Li, T. Yang, B. H. Li, Z. Z. Zhang, C. X. Shan, J. Y. Zhang, and D. Z. Shen, J. Cryst. Growth **312**, 1813 (2010).
https://doi.org/10.1016/j.jcrysgro.2010.02.042
77. H. L. Tan, C. Yi. Jia, X. X. Ge, and Ch. Xiang, Adv. Mater. Res. (Durnten-Zurich, Switz.) **468–471**, 1726 (2012).
https://doi.org/10.4028/www.scientific.net/amr.468-471.1726
78. M. K. Gupta, N. Sinha, and B. Kumar, J. Appl. Phys. **109**, 83532 (2011).
https://doi.org/10.1063/1.3574656
79. G. H. Kim, B. D. Ahn, D. L. Kim, K. H. Jung, and S. Y. Lee, Proc. SPIE **6474**, 647409 (2007).
https://doi.org/10.1117/12.699613
80. M. A. Myers, V. Khranovskyy, J. Jian, J. H. Lee, H. Wang, and H. Wang, J. Appl. Phys. **118**, 65702 (2015).
https://doi.org/10.1063/1.4928183
81. V. V. S. Kumar, D. Kanjilal, J. Chin. Adv. Mater. Soc. **2** 199 (2014).
https://doi.org/10.1016/j.jphotochem.2013.11.002
82. L. Xu, J. Miao, Yu. Chen, J. Su, M. Yang, L. Zhang, L. Zhao, and Sh. Ding, Optik **170**, 484 (2018).
https://doi.org/10.1016/j.ijleo.2018.06.016
83. Zh. Zhou, Yi. Pei, J. Zhao, G. Fu, and X. Yan, Appl. Phys. Lett. **118**, 191103 (2021).
https://doi.org/10.1063/5.0047403
84. J.-H. He, J.-J. Ke, P.-H. Chang, K.-T. Tsai, P. C. Yang, and I. M. Chan, Nanoscale **4**, 3399 (2012).
https://doi.org/10.1039/c2nr30688c
85. D. Wang, J. Zhou, and G. Liu, J. Alloys Compd. **481**, 802 (2009).
https://doi.org/10.1016/j.jallcom.2009.03.111

86. H. Ahmoum, M. Boughrara, M. S. Su'ait, and M. Kerouad, Chem. Phys. Lett. **719**, 45 (2019). https://doi.org/10.1016/j.cplett.2019.01.032

87. Y. J. Zeng, Z. Z. Ye, J. G. Lu, W. Z. Xu, L. P. Zhu, B. H. Zhao, and S. Limpijumnong, Appl. Phys. Lett. **89**, 42106 (2006). https://doi.org/10.1063/1.2236225

88. P. Chand, A. Gaur, A. Kumar, and U. K. Gaur, Ceram. Int. **40**, 11915 (2014). https://doi.org/10.1016/j.ceramint.2014.04.027

89. Q. X. Wan, J. Yi. Chen, Zh. H. Xiong, D. M. Li, B. L. Shao, and G. D. Liu, Advanced Materials Research **535–537**, 214 (2012). https://doi.org/10.4028/www.scientific.net/amr.535-537.214

90. R. Rakkesh and S. Balakumar, Process. Appl. Ceram. **8**, 7 (2014). https://doi.org/10.2298/pac1401007r

91. B. Wang, L. Tang, J. Qi, H. Du, and Zh. Zhang, J. Alloys Compd. **503**, 436 (2010). https://doi.org/10.1016/j.jallcom.2010.05.028

92. R. Chowdhury, S. Adhikari, and P. Rees, Phys. B: Condens. Matter (Amsterdam, Neth.) **405**, 4763 (2010). https://doi.org/10.1016/j.physb.2010.08.072

93. R. T. Mendi, S. M. Elahi, and M. R. Abolhassani, Mod. Phys. Lett. B **28**, 1450139 (2014). https://doi.org/10.1142/s0217984914501395

94. R. T. Mendi, S. M. Elahi, and M. R. Abolhassani, Mod. Phys. Lett. B **28**, 1450243 (2014). https://doi.org/10.1142/s0217984914502431

95. M. Riju Khandaker, M. Kamruzzaman, R. Afrose, M. Rahman, M. K. R. Khan, M. N. H. Liton, M. A. Helal, T. K. Anam, and M. M. Rahman, Crystallogr. Rep. **65**, 968 (2020). https://doi.org/10.1134/s1063774520060188

96. M. Fox, *Optical Properties of Solids* (Oxford University Press, New York, 2001).

97. L. Guan, B. Liu, Q. Li, Ya. Zhou, J. Guo, G. Jia, Q. Zhao, Yi. Wang, and G. Fu, Phys. Lett. A **375**, 939 (2011). https://doi.org/10.1016/j.physleta.2010.12.064

98. Z. Chun-Ying, W. Jing, and B. Yue-Lei, Chin. Phys. B **19**, 047101 (2010). https://doi.org/10.1088/1674-1056/19/4/047101